

Politecnico di Bari

Repository Istituzionale dei Prodotti della Ricerca del Politecnico di Bari

Tsunamis generated by landslides at the coast of conical islands: experimental benchmark dataset for mathematical model validation

This is a post print of the following article

Original Citation:
Tsunamis generated by landslides at the coast of conical islands: experimental benchmark dataset for mathematical model validation / Romano, A., DI RISIO, M., Bellotti, G., Molfetta, M.G., Damiani, L., De Girolamo, P.. - In: LANDSLIDES. - ISSN 1612-510X. - 13:6(2016), pp. 1379-1393. [10.1007/s10346-016-0696-4]

Availability:
This version is available at http://hdl.handle.net/11589/110117 since: 2021-03-05

Published version
DOI:10.1007/s10346-016-0696-4

Publisher:

Terms of use:

(Article begins on next page)

17 November 2026

This is the author produced postprint of the paper

Tsunamis generated by landslides at the coast of conical islands: experimental benchmark dataset for mathematical model validation

by Alessandro Romano[1]*, Marcello Di Risio[2], Bellotti, G.[3], Molfetta, M. G.[4], Damiani, L.[5], Paolo De Girolamo[6]

[1]*Post Doc Researcher, "Sapienza", University of Rome, Rome, Italy*
[2]*Researcher, University of L'Aquila, L'Aquila, Italy*
[3]*Associate Professor, Third University of Rome, Rome, Italy*
[4]*Researcher Assistant, Polytechnic University of Bari, Bari, Italy*
[5]*Full Professor, Polytechnic University of Bari, Bari, Italy*
[6]*Associate Professor, "Sapienza", University of Rome, Rome, Italy*
*__Corresponding author__: alessandro.romano@uniroma1.it

Please, cite this work as follows:

Romano, A., Di Risio, M., Bellotti, G., Molfetta, M.G., Damiani, L., De Girolamo, P. Tsunamis generated by landslides at the coast of conical islands: experimental benchmark dataset for mathematical model validation, Landslides (2016), ISSN 1612-5118, http://dx.doi.org/10.1007/s10346-016-0696-4

Publisher link and Copyright information:

You can download the original paper from: http://dx.doi.org/10.1007/s10346-016-0696-4
©Springer-Verlag Berlin Heidelberg 2016



This work is licensed under the Creative Commons Attribution-NonCommercial-NoDerivatives 4.0 International License. To view a copy of this license, visit http://creativecommons.org/licenses/by-nc-nd/4.0/ or send a letter to Creative Commons, PO Box 1866, Mountain View, CA 94042, USA.

Licensees may copy, distribute, display and perform the work and make derivative works and remixes based on it only if they give the author or licensor the credits (attribution) in the manner specified by these.

Licensees may copy, distribute, display, and perform the work and make derivative works and remixes based on it only for non-commercial purposes.

Licensees may copy, distribute, display and perform only verbatim copies of the work, not derivative works and remixes based on it.

Landslides
DOI: 10.1007/s10346-016-0696-4

Tsunamis generated by landslides at the coast of conical islands: experimental benchmark dataset for mathematical model validation

Alessandro Romano[1]*, Marcello Di Risio[2], Bellotti, G.[3], Molfetta, M. G.[4], Damiani, L.[5], Paolo De Girolamo[6]

Abstract
This paper presents a new experimental campaign aimed at reproducing tsunamis generated by landslides at the flank of conical islands. In order to describe in high details the wave field around the island a special acquisition system, which consists of both fixed and movable wave gauges, has been employed. Indeed, each experiment has been repeated several times by changing the configuration of the movable gauges, then obtaining a single virtual experiment with high spatial resolution measurements. Fixed run-up gauges measure the waves at fixed locations to statistically quantify the repeatibility of the experiments. Selected experimental results are illustrated within the paper, that is mainly aimed at defining a benchmark dataset, available on request, for the development/calibration/validation of analytical and numerical models of tsunamis generated by landslides.

Keywords
Landslide Tsunamis, Physical Modelling, Water waves

[1]*Post Doc Researcher, "Sapienza", University of Rome, Rome, Italy*
[2]*Researcher, University of L'Aquila, L'Aquila, Italy*
[3]*Associate Professor, Third University of Rome, Rome, Italy*
[4]*Researcher Assistant, Polytechnic University of Bari, Bari, Italy*
[5]*Full Professor, Polytechnic University of Bari, Bari, Italy*
[6]*Associate Professor, "Sapienza", University of Rome, Rome, Italy*
***Corresponding author**: alessandro.romano@uniroma1.it

1. Introduction

When either subaerial or submerged landslides occur, the displacements at water body boundaries generate transient free surface perturbations. The involved phenomena are quite different with respect to earthquake generated tsunamis. In the case at hand, the tsunami source, i.e. the landslide, takes place on both larger temporal- and smaller spatial-scale (e.g. Di Risio and Sammarco, 2008). Indeed, the land deformations are of the order of hundreds of meters and the generated waves are different from those induced by submarine earthquakes. Conversely, as far as tsunamis generated by fault deformations are considered, the land deformations can be in the order of tens to hundreds kilometers. Landslide tsunamis tend to be a local phenomenon, although extreme (Synolakis et al, 2002). The events occurred at Lituya Bay (Alaska, July 9, 1958; e.g. Miller, 1960; Fritz et al, 2009) and at the Vajont Valley (Italy, October 9, 1963; e.g. Panizzo et al, 2005) are meaningful examples of such a phenomenon. When the landslide occurs directly at the water body boundaries, impulse waves both radiate seaward and propagate along the boundary itself. Therefore the complex interaction that exists between the generation and the propagation mechanisms has to be taken into account. In such a case trapped waves can be triggered and propagate along the coast by inducing large wave run-up observed in some real cases (Ursell, 1952; Liu and Yeh, 1996; Liu et al, 1998; Johnson, 2007; Bellotti et al, 2009).

The first attempt to analyze wave propagation alongshore in the case of an ideal circular island was motivated by the extreme inundation observed in the rear side of Babi Island (Indonesia) during an earthquake induced tsunami attack (December 12, 1992). A series of experiments was performed (e.g. Yeh et al, 1994; Briggs et al, 1995a,b; Liu et al, 1995; Cho and Liu, 1999; Cho et al, 2004) aimed at defining inundation maps around a circular island due to the attack of a solitary wave propagating from offshore. Also when transient waves are generated directly on the shore they may remain trapped close to the coast due to refraction phenom-

ena and edge waves occur (Ursell, 1952; Lynett and Liu, 2005; Johnson, 2007; Romano et al, 2013). Recently the problem of wave generation due to coastal tsunamigenic sources, i.e. coastal landslides, has been tackled by means of theoretical (Sammarco and Renzi, 2008; Renzi and Sammarco, 2010), experimental (e.g. Di Risio et al, 2009a,b; Mohammed and Fritz, 2012) and numerical modeling (e.g. Cecioni et al, 2011; Montagna et al, 2011) in the case of both straight coast and circular island.

This paper presents a new experimental campaign aimed at reproducing tsunamis generated by landslides at the flank of ideal conical islands. The research is based on the previous experimental study of Di Risio et al (2009b), that provided a detailed analysis of the tsunamis run-up at the coast of the island, focusing on subaerial landslides, and of Romano et al (2013) that studied the alongshore propagation of the tsunamis, pointing out that the waves propagate around the island as a 0th-order edge wave packet.

The main aim of the present paper consists in providing an experimental benchmark dataset for validating analytical and numerical models due to the high spatial resolution measurements, that allow to describe in high details the pattern of generated waves that propagate both around the island (i.e. trapped waves) and far from the coasts (i.e. radiating waves). In order to achieve high spatial resolution measurements a special movable acquisition system, the same described by Romano et al (2013), has been employed, along with a series of fixed wave gauges. Each experiment has been repeated 37 times by changing the configuration of the movable gauges devoted at measuring the water free surface elevation around the island. It is worth noticing that the spatial resolution of the collected data is comparable to that obtained by mathematical models.

Surface elevation gauges and run-up gauges were kept fixed, thus an in-depth statistical analysis of the experimental repeatability has been carried out and it is presented in the paper. Moreover, with respect to the previous research (Di Risio et al, 2009b; Romano et al, 2013) a better description of the waves that propagate away from the coast is presented. Finally, it is important to stress that a further new landslide model has been tested by allowing comparison of the effect of landslide thickness (i.e. landslide volume) while keeping constant other parameters.

The paper is structured as follows. The next section details the new experimental layout; the succeeding section illustrates the procedure for characterize the landslide kinematic. Then runup and elevation time series are analyzed. Concluding remarks close the paper.

2. The experimental layout

The experiments have been carried out in a large wave tank (50 m long, 30 m wide, 3 m deep) at the Research and Experimentation Laboratory for Coastal Defence of Polytechnic of Bari (LIC, Italy). A truncated conical island (base diameter equal to 8.90 m, maximum height equal to 1.20 m, see Figure 1) made up of PVC (i.e. Polyvinyl chloride) sheets (thickness 0.01 m) sustained by a rigid steel frame was placed in the centre of the tank. The water depth was kept constant to 0.80 m (undisturbed shoreline radius $R_0 = 2.05$ m). The slope (α) of the island flanks was kept constant to $\cot\alpha = 3$ (i.e. 1 vertical, 3 horizontal) in order to reproduce the typical slope of volcanic islands where landslides are likely to occur (i.e. Stromboli Island, Southern Tyrrhenian Sea, Italy, Tinti et al, 2005).

In order to reproduce the effect of landslides, past studies were carried out by using solid boxes falling vertically (Scott Russell's wave generator; Russell, 1845; Yim et al, 2008; Di Risio et al, 2011) or sliding along inclines with different shapes (semi-elliptical, triangular, parallelepiped) with deformable sand bags and with granular landslide model is used, its shape has to be defined preliminarily, and the deformations and porosity of real landslides are not accounted for in the model. Grilli and Watts (2003) and Watts et al (2005) found that, in the case of underwater landslides, the higher the spreading of a Gaussian shape, the lower the amplitude of the generated waves. Then, Watts et al (2005) indicates that semi-elliptical shaped rigid body represents the worst case scenarios, at least for underwater landslides (Watts, 2000; Enet and Grilli, 2007; Di Risio et al, 2009a,b). Furthermore, the landslide shape has preferable to be analytically reproduced in order to model it within mathematical models. Then, as in Di Risio et al (2009a,b), landslide models shaped as a half of an ellipsoid was used (Figure 2).

In a reference frame with the origin placed at the centre of the ellipsoid, the landslide model is described by the following equation:

$$x^2/a^2 + y^2/b^2 + z^2/c^2 = 1 \tag{1}$$

where x is the coordinate directed along the incline, y the coordinate parallel to the (local) undisturbed shoreline and z is the orthogonal distance from island flank. The axis a (orthogonal to the local undisturbed shoreline) is equal to 0.40 m (landslide length $2a = 0.80$ m), the axis b (parallel to the local undisturbed shoreline) is equal to 0.20 m (landslide width $2a = 0.40$ m).

During the experiments two different landslide models were used. The first one (hereinafter referred to as LS1) is characterized by a thickness of 0.05 m (c=0.05

Wave Gauges			Runup Gauges		Ultrasound sensors		
Sensor name	Radial Position (R) (m)	Angular Position (θ) (°)	Sensor name	Angular Position (θ) (°)	Sensor name	Radial Position (R) (m)	Angular Position (θ) (°)
7WG	4.53	7.9	1RG	14.5	1WG	5.92	0 to 180 by 5
8WG	4.08	8.9	2RG	20.6	2WG	5.62	0 to 180 by 5
9WG	3.66	10.0	3RG	34.3	3WG	5.32	0 to 180 by 5
10WG	3.13	11.9	4RG	47.6	4WG	5.02	0 to 180 by 5
			5RG	60.2	5WG	4.72	0 to 180 by 5
			6RG	72.9	6WG	4.42	0 to 180 by 5
			7RG	86.3	1US	3.88	0 to 180 by 5
			8RG	98.7	2US	3.48	0 to 180 by 5
			9RG	111.5	3US	3.08	0 to 180 by 5
			10RG	125.2	4US	2.78	0 to 180 by 5
			11RG	138.6	5US	2.58	0 to 180 by 5
			12RG	151.6	6US	2.43	0 to 180 by 5
					7US	2.28	0 to 180 by 5

Table 1. Sensors position and naming.

m). The LS1 volume is then equal to $V = 0.0084$ m^3. The thickness of the second landslide model (hereinafter referred to as LS2) is 0.10 m (c=0.10 m) and the volume $V = 0.0168$ m^3. The density of the landslide models was kept constant to 1.83 kg/m^3 for a total mass of about 15.4 kg and 31.7 kg for LS1 and LS2 respectively.

The landslide models are made up of PVC covered by an exterior layer of fiberglass. The flat bottom, in contact with the island flank, is made up of steel. In order to constrain the landslide to move along a fixed line a steel T frame is welded to the landslide bottom (see cross sections of Figure 2).

The experiments aim at measuring the waves generated by the landslide model that slides down the island flank. Then landslide motion and water surface elevation data have to be collected.

A high-resolution camera was placed on a steel frame placed just outside of the wave tank, directly in front of the generation area (see Figure 1). The digital images collected by means of the video-camera have been analyzed in order to reconstruct the landslide motion, as detailed in the next section. In order to measure the water level around the conical island wave gauges (hereinafter referred to as WG), ultrasound water level sensors (hereinafter referred to as US) and run-up gauges (hereinafter referred to as RG) were employed. As already anticipated, some of the sensors were kept fixed in space. A series of level gauges (both WG and US) was placed on a steel frame that can rotate around the island centre spanning a half of the island (see Figure 1). This "movable" system allows to collect the free surface time series along cross-shore sections, starting from the axis along which the landslide moves (θ =0) up to the rear side of the island (θ =180). For each test, the landslide is placed at starting position and the movable steel frame moved to the correct angular position, then the acquisition process begins, the landslide model is released and the tsunami is generated. Typically the acquisition process was stopped about 50 s after the release of the landslide, as the waves reflected at the side walls completely influence the wave field. The procedure was repeated for each position of the movable frame, from θ =0 up to θ =180 every 5, for a total of 37 landslide releases. The fixed sensors were used to check the repeatability of the tests; the sensors placed on the movable frame were used to measure the whole wave pattern around the island. In particular: (a) 12 run-up gauges were embedded directly into the PVC of the island flanks in order to measure the shoreline displacements time series; (b) 9 wave gauges were placed in fixed position near the generation area and in the far field; (c) 7 ultrasound sensors and 6 wave gauges were placed on the movable frame. Table 1 summarizes the sensors location and naming. Once the repeatability of the tests have been addressed, the whole datasets (37 landslide releases) corresponds to a unique test with

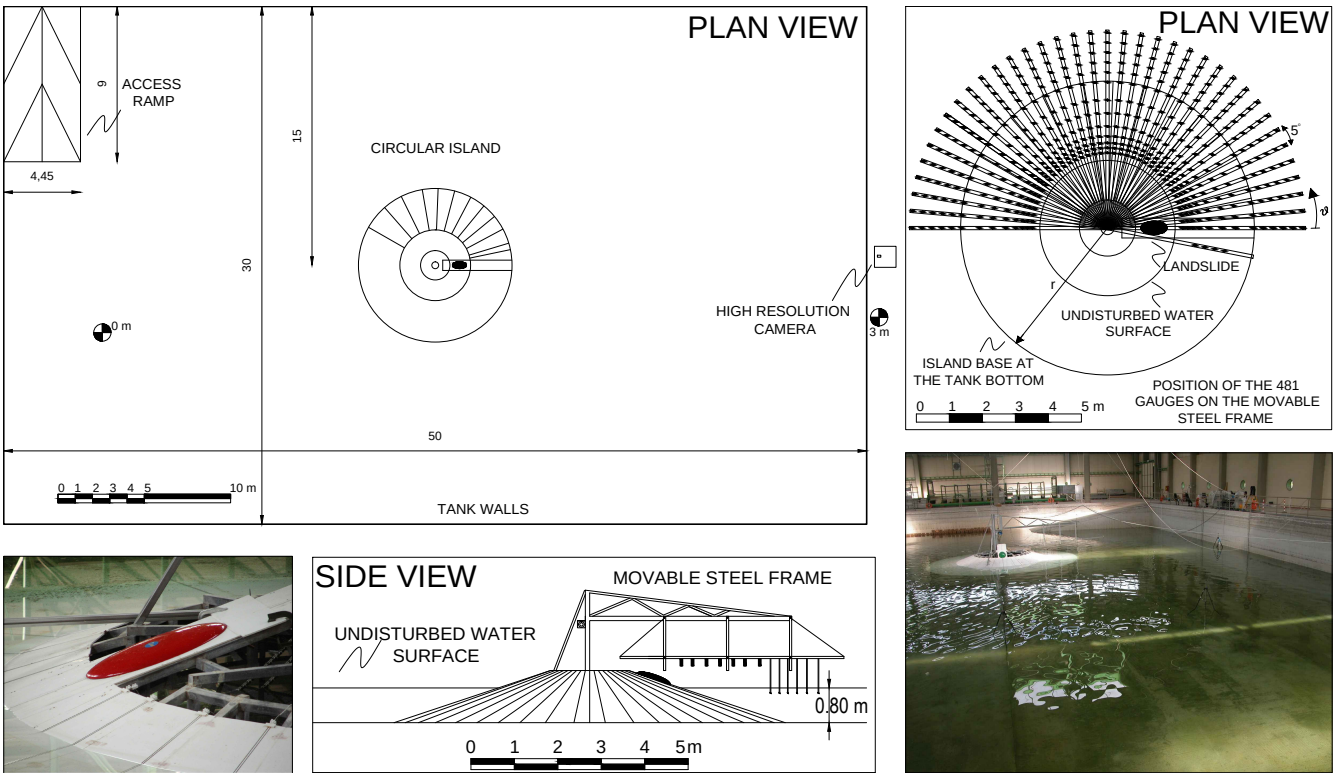


Figure 1. Sketch of the experimental layout, adapted from Romano et al (2013) (measures in meters).

more than 500 sensors. The obtained high spatial resolution (comparable to numerical results, e.g. Montagna et al, 2011) allows to experimentally characterize the wave pattern around the island.

3. Landslide motion

The proper description of the landslide kinematic is a crucial point when experimental data are intended to be used as benchmark test case for mathematical models validation. The governing equation of landslide motion has been widely used in past researches in the case of submerged landslides (e.g. Pelinovsky and Poplavsky, 1996; Watts, 1998). In the followings the methodology used to estimate the parameters needed to reproduce the observed landslide motion in the case of subaerial landslides is illustrated.

During the subaerial phase, the motion is governed by the following equation:

$$m\frac{d^2s}{dt^2} = mg\left(\sin\alpha - C_n\cos\alpha\right), \tag{2}$$

where m is the landslide mass, s the landslide displacements, t the elapsed time, g the gravity acceleration, α the incline slope angle, C_n the Columbic friction coefficient. Then, if landslide displacements are measured and velocities estimated by numerical differentiation, the Columbic friction coefficient can be inferred by using the following relationship:

$$C_n = \left(1 - \frac{u_0^2}{2gz_0}\right)\tan\alpha, \tag{3}$$

where u_0 indicates the landslide velocity when it hits the free surface and z_0 the dropping height, measured along the vertical direction. When the landslide hits the free surface a transition phase begins, during which the landslide motion is affected by the complex interaction between the landslide and the fluid flow, related to the water entry problem. Once the landslide becomes totally submerged buoyancy and drag forces act on it. During the underwater travel the landslide motion is governed by the following equation:

$$\begin{aligned}(m + C_m m_0)\frac{d^2s}{dt^2} \quad &= \quad (m - m_0)\,g\,(\sin\alpha - C_n\cos\alpha) + \\ &-\frac{1}{2}C_d\rho A\left(\frac{ds}{dt}\right)^2\end{aligned} \tag{4}$$

where C_m is the added mass coefficient, m_0 is the displaced water mass, A is the main cross section of the moving landslide (i.e. perpendicular to the direction of motion), ρ is the water density. The global drag coefficient C_d describes both form drag and skin friction:

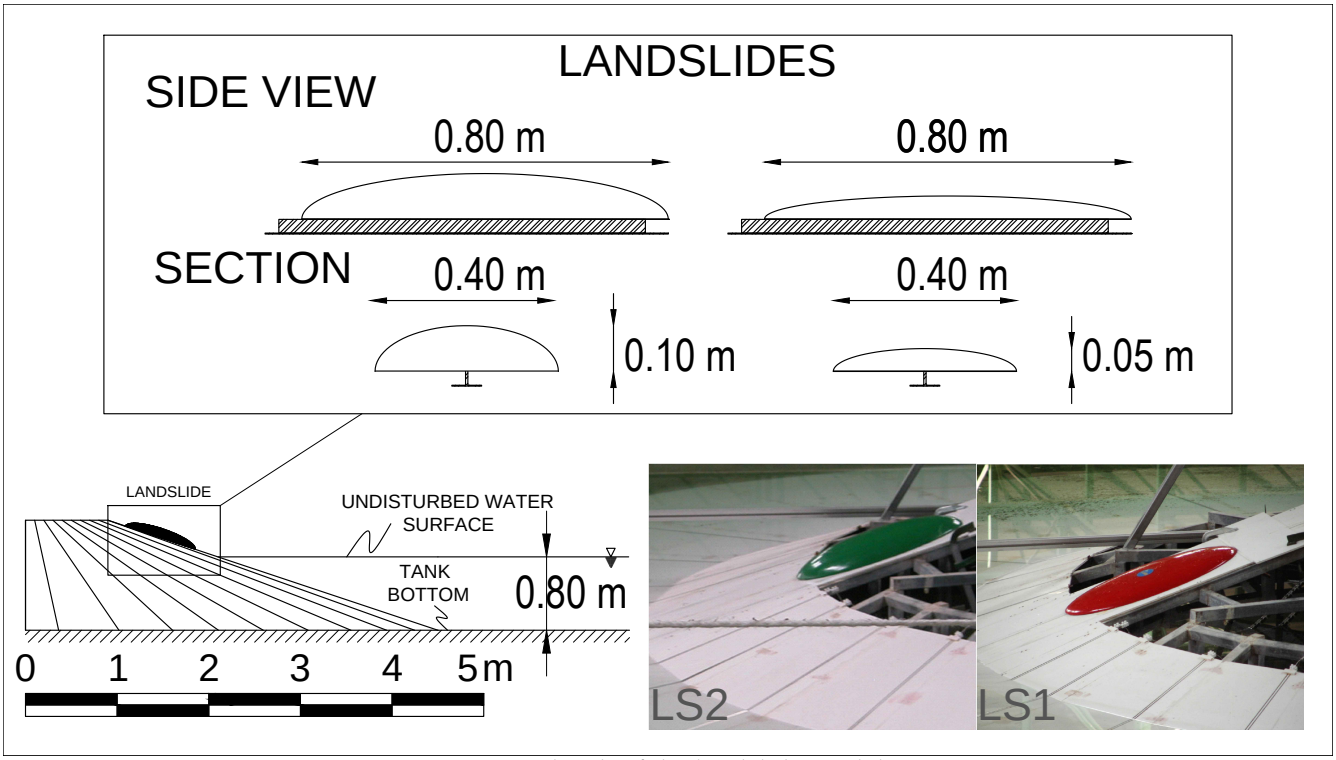


Figure 2. Sketch of the landslide models.

$$C_d = \frac{C_F A_w}{A} + C_D \tag{5}$$

where C_D, C_F and A_w are the form drag coefficient, the skin friction coefficient and the wetted surface respectively.

For LS1 Di Risio et al (2009a) performed a detailed analysis of the landslide motion on the basis of acceleration measurements collected by means of an accelerometer placed into the landslide model.

Due to the different scale of the experiments and to the related experimental difficulties in managing the connection cable of the accelerometer, as anticipated, the landslide motion were reconstructed on the basis of the analysis of a series of digital images collected by means of a high resolution videocamera (images frequency acquisition equal to 25 Hz). The collected images were rectified based on a series of points whose positions in space were measured by means of a high precision topographic total station. Then the influence of image distorsion due to water refraction is minimized. All the images were analyzed to reconstruct the instantaneous position of the landslide from which the displacements time series is defined.

In the case of submerged landslides the theoretical solution of (4) is (e.g. Watts, 1998):

$$s(t) = \frac{u_t^2}{a_0} \log\left[\cosh\left(\frac{a_0 t}{u_t}\right)\right] + s_0 \tag{6}$$

where a_0 is the initial acceleration and u_t is the terminal velocity that the landslide reaches when the gravity action is balanced by the boyancy, friction and drag forces. For submerged landslides, the initial acceleration a_0 can be directly inferred from (4) by imposing the velocity to be zero at the initial time:

$$a_0 = \frac{(m - m_0) g (\sin\alpha - C_n \cos\alpha)}{m + C_m m_0}. \tag{7}$$

Similarly, the terminal velocity is the (constant) velocity at which the landslide moves with a nil force resultant (i.e. $d^2s/dt^2 = 0$):

$$u_t^2 = \frac{2(m - m0) g (\sin\alpha - C_n \cos\alpha)}{C_d \rho A}. \tag{8}$$

It has to be stressed that the solution (6) with a_0 and u_t provided by (7) and (8) respectively, is valid only when the landslide motion starts when it is totally submerged. However such a solution may be adopted also in the case of subaerial landslide if different initial conditions are considered. Indeed equation (4) is valid for

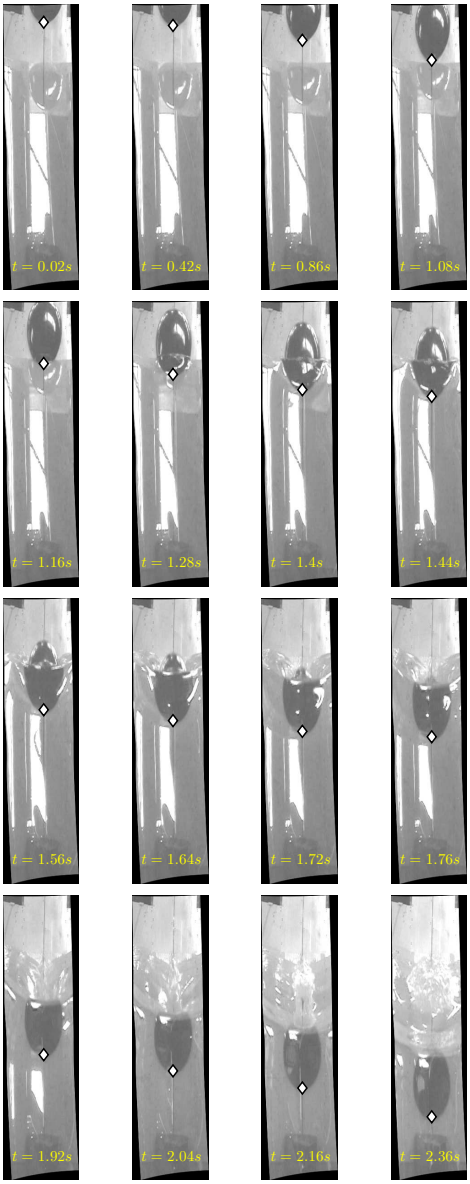


Figure 3. Example of the image analysis for tracking landslide motion: each panel shows the landslide at a given time-step after the release; the white diamond marker identifies the position of the seaward edge of the landslide.

the submerged phase of both subaerial and submerged landslide. When the transition phase ends, the landslide motion is governed by equation (4) and the initial velocity may be rougly estimated by using equation (2), say it u_0^*. In the case of subaerial landslide, the solution for the underwater phase ($t > t_0$, being t_0 the instant when the transition phase ends) can be expressed in terms of velocity:

$$v(t) = u_t \tanh\left(\frac{a_0^* t}{u_t}\right) \quad t > t_0 \tag{9}$$

with

$$t_0 = \frac{u_t}{a_0^*} \tanh^{-1}\left(\frac{a_0^*}{u_t}\right) \tag{10}$$

The acceleration a_0^*, given by equation (7), is not the initial acceleration of the real landslide, but that of a kind of "equivalent submerged landslide" that reaches the velocity u_0 at instant $t = t_0$. It has to be noticed that terminal velocity of the "dummy" equivalent submerged landslide is equal to that one of the real subaerial landslide.

In order to estimate the values of u_t and a_0^* it is possible to use a least square optimization technique based on observed landslide displacements.
The falling height z_0 was kept constant during the experiments (z_0= 0.14 m), then the value of impact velocity u_0 (almost the same for all the tests) was used to estimate the Columbic friction coefficient (C_n).
In order to estimate the values of C_d and C_m, the landslide displacements time series related to underwater phase were used. In particular, the terminal velocity u_t and initial acceleration a_0^* are inferred by means of non linear least square optimization (Gauss-Newton method) aimed at minimizing the deviation between the computed and observed displacements.

4. Experimental findings and discussion

This section describes the experimental results in terms of landslide motion and of free surface elevations collected all around the conical island and wave runup at its coast. In particular, once the repeatibility of the tests is addressed, the data are analyzed in order to describe the wave characteristics.

4.1 Landslide motion measurements

By means of image analysis techniques based on the colour identification in rectified pictures, it was possible to track the position of the landslide (see Figure 3).
The analysis described previously provides landslides displacements rather than its accelerations. In order to infer motion parameters (i.e. C_d, C_m and C_n) it is possible to estimate landslide accelerations by double numerical differentiation of displacements. However the double differentiation may lead to numerical errors on acceleration estimation. Then a different approach to infer the dynamical coefficients was employed. In particular, the Columbic friction coefficient (C_n) was estimated on the basis of estimated velocity, whilst the added mass and the global drag coefficients were estimated directly from the observed landslide displacements.
Data analysis showed that C_n is equal to 0.206 ($\pm$0.002, $R^2 = 0.998$). The related impact velocity was then estimated as 1.023 m/s ($\pm$0.007). Di Risio et al (2009a)

used the landslide model LS1 and they analyzed the accelerations time series by obtaining an impact velocity of 0.9962 m/s, about 2.5% lower than, then consistent to, the result presented herein. The drag coefficient C_d were estimated as 0.40 and 0.47 for LS1 and LS2 respectively (± 0.006). The added mass coefficient C_m were estimated as 0.26 and 0.51 for LS1 and LS2 respectively (± 0.011).

4.2 Repeatibility

As described in section 2, some of the deployed sensors were kept in a fixed position in order to verify the tests repeatibility.

Figure 4 shows the results of standard zero-crossing analysis on the runup time series collected by means of RGs. The upper panel shows the maximum induced tsunami runup (positive values) and maximum drawdown (negative values) all around the island as a function of the dimensionless distance s' from generation area ($s' = R_0\theta/b$). Note that in Figure 4, just for graphical reasons, positive values of s' refer to experimental results observed for LS1, while negative ones to LS2 data. The four lower panels show the same results for the first four waves of the generated wave packet. The markers used for maximum runup and drawdown indicate which wave of the packet induces it (circles for the first wave, squares for the second one, diamonds for the third one and triangles for the fourth one). In the lower panels the individual experimental data are reported as a black point, their average values are indicated by a blue segment and the 95% confidence interval is reported by red segments. Generally speaking, the repeatibility is satisfactory especially for the first wave. Mean values and confidence intervals, evaluated at each run-up gauge for both LS1 and LS2, are listed in Tables 2, 3, 4 and 5.

However, it is clearly observable that when the wave runup, or wave drawdown, reaches its maximum the repeatibility deteriorates. This aspect was already highlighted by Di Risio et al (2009b). Therefore it is confirmed that small differences in the landslide energetic features (i.e. drop height) can lead to some difference in terms of maximum runup and drawdown, i.e. on the envelope amplitude. The differences in terms of envelope amplitude increase with increasing volume. This is related to several aspects, e.g. the dispersive features of the generated waves that propagate along the coastline, the trapping mechanisms and the nonlinear effects related to the water entry problem. Furthermore it can be observed that (i) the confidence interval of wave runup is wider than that of wave drawdown and (ii) the confidence intervals are wider for the larger landslide model (i.e. LS2).

In conclusion, it can be observed that in general the experiments show a satisfactory repeatibility.

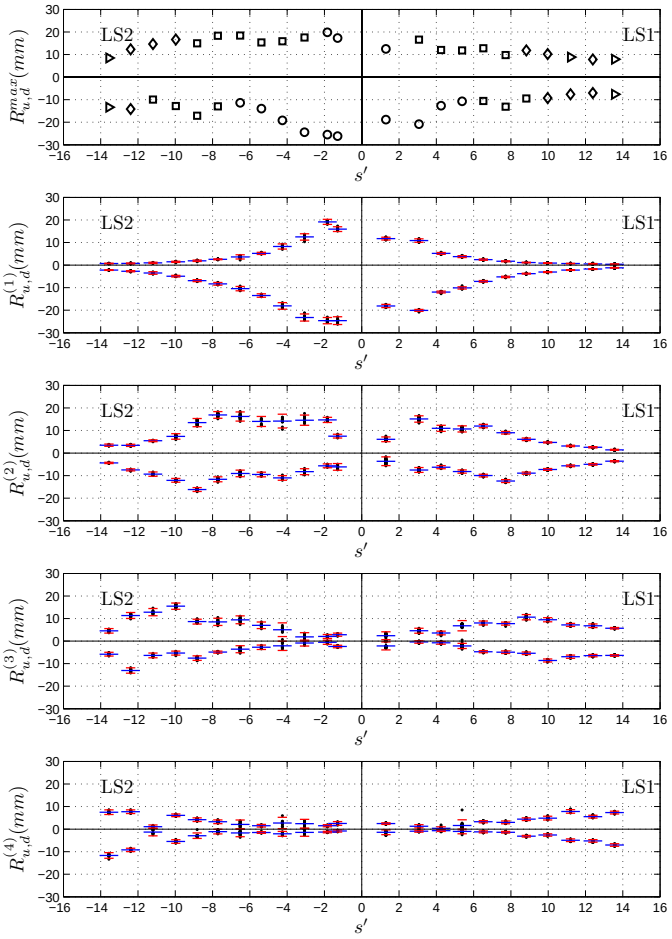


Figure 4. Observed runup and drawdown as a function of dimensionless distance from generation area. Upper panel: maximum runup (R_u) and maximum rundown (R_d). Markers indicates which waves of the generated packet induces maximum runup and drawdown (circles if the first wave, squares if the second one, diamonds if the third one, triangle if the fourth one). Lower panels: runup ($R_u^{(i)}$) and drawdown ($R_d^{(i)}$) induced by the i-th wave of the generated packet. Black points indicate the single test experimental data, blue segments the mean values and red segments the confidence intervals (0.95 confidence level).

4.3 Wave amplitudes

Further inspection of Figure 4 allows to describe the tsunami features in terms of wave runup and drawdown. The influence of the landslide volume is clear: the larger the volume, the larger the induced runup and drawdown (in absolute value). Consistently with Di Risio et al (2009b) and Lynett and Liu (2005), it is noted that the maximum runup and the maximum run-

LS1								
GAUGES	$\overline{R}_u^{(1)}$ (mm)	95% CI (mm)	$\overline{R}_u^{(2)}$ (mm)	95% CI (mm)	$\overline{R}_u^{(3)}$ (mm)	95% CI (mm)	$\overline{R}_u^{(4)}$ (mm)	95% CI (mm)
1RG	11.73	± 0.62	6.10	± 1.04	2.38	± 1.74	2.44	± 0.36
2RG	-	± -	-	± -	-	± -	-	± -
3RG	10.88	± 0.76	15.09	± 1.41	4.58	± 1.10	1.26	± 0.70
4RG	5.16	± 0.41	10.96	± 1.32	3.58	± 0.82	0.34	± 0.66
5RG	3.74	± 0.42	10.69	± 1.35	6.81	± 2.29	1.59	± 2.53
6RG	2.41	± 0.28	11.95	± 0.74	8.02	± 0.85	3.27	± 0.49
7RG	1.67	± 0.21	8.98	± 0.57	7.75	± 0.66	3.00	± 0.61
8RG	1.13	± 0.14	6.09	± 0.56	10.59	± 1.16	4.41	± 0.59
9RG	0.89	± 0.13	4.69	± 0.25	9.44	± 0.90	4.87	± 0.83
10RG	0.67	± 0.13	3.13	± 0.31	7.16	± 0.68	7.82	± 0.78
11RG	0.49	± 0.19	2.55	± 0.29	6.79	± 0.82	5.51	± 0.63
12RG	0.38	± 0.14	1.43	± 0.21	5.68	± 0.32	7.35	± 0.62

Table 2. Mean values and confidence intervals of run-up (LS1).

LS1								
GAUGES	$\overline{R}_d^{(1)}$ (mm)	95% CI (mm)	$\overline{R}_d^{(2)}$ (mm)	95% CI (mm)	$\overline{R}_d^{(3)}$ (mm)	95% CI (mm)	$\overline{R}_d^{(4)}$ (mm)	95% CI (mm)
1RG	-18.14	± 0.72	-3.60	± 1.94	-2.10	± 1.76	-1.40	± 1.04
2RG	-	± -	-	± -	-	± -	-	± -
3RG	-20.08	± 0.44	-7.50	± 1.07	-0.40	± 0.54	-0.90	± 0.42
4RG	-11.95	± 0.39	-6.20	± 0.70	-0.70	± 0.61	-0.60	± 0.37
5RG	-10.11	± 0.50	-8.10	± 0.72	-2.10	± 1.14	-1.00	± 1.04
6RG	-7.20	± 0.34	-9.90	± 0.59	-4.70	± 0.45	-1.20	± 0.44
7RG	-5.20	± 0.31	-12.40	± 0.64	-4.90	± 0.57	-1.30	± 0.35
8RG	-3.70	± 0.21	-8.90	± 0.49	-5.30	± 0.55	-3.10	± 0.35
9RG	-3.10	± 0.20	-7.20	± 0.40	-8.50	± 0.66	-2.50	± 0.52
10RG	-2.20	± 0.18	-5.60	± 0.37	-6.90	± 0.70	-4.90	± 0.62
11RG	-1.70	± 0.16	-5.00	± 0.37	-6.40	± 0.52	-5.20	± 0.57
12RG	-1.20	± 0.15	-3.60	± 0.25	-6.30	± 0.35	-7.00	± 0.56

Table 3. Mean values and confidence intervals of drawdown (LS1).

LS2								
GAUGES	$\overline{R}_u^{(1)}$ (mm)	95% CI (mm)	$\overline{R}_u^{(2)}$ (mm)	95% CI (mm)	$\overline{R}_u^{(3)}$ (mm)	95% CI (mm)	$\overline{R}_u^{(4)}$ (mm)	95% CI (mm)
1RG	15.94	± 1.05	7.48	± 0.84	2.83	± 0.68	2.51	± 0.82
2RG	19.14	± 1.12	14.69	± 1.12	2.05	± 0.88	1.48	± 0.47
3RG	12.48	± 1.40	14.55	± 2.26	1.87	± 1.87	2.38	± 1.92
4RG	8.24	± 1.13	14.14	± 3.05	5.03	± 3.02	2.71	± 2.49
5RG	5.19	± 0.48	13.99	± 2.21	6.98	± 1.46	1.49	± 0.56
6RG	3.62	± 0.93	16.20	± 2.03	9.42	± 1.74	2.08	± 1.92
7RG	2.56	± 0.20	16.87	± 1.48	8.52	± 1.59	3.25	± 0.84
8RG	1.90	± 0.30	13.500	± 1.81	8.63	± 1.07	4.17	± 0.81
9RG	1.44	± 0.25	7.36	± 1.21	15.50	± 1.38	6.11	± 0.60
10RG	0.96	± 0.28	5.46	± 0.40	12.82	± 1.61	1.09	± 0.72
11RG	0.72	± 0.22	3.43	± 0.47	11.33	± 1.31	7.72	± 0.82
12RG	0.68	± 0.13	3.47	± 0.50	4.55	± 0.99	7.49	± 1.01

Table 4. Mean values and confidence intervals of run-up (LS2).

LS2								
GAUGES	$\overline{R}_d^{(1)}$ (mm)	95% CI (mm)	$\overline{R}_d^{(2)}$ (mm)	95% CI (mm)	$\overline{R}_d^{(3)}$ (mm)	95% CI (mm)	$\overline{R}_d^{(4)}$ (mm)	95% CI (mm)
1RG	-24.63	± 1.71	-6.10	± 1.48	-2.40	± 0.55	-0.80	± 0.46
2RG	-24.62	± 1.36	-5.60	± 0.85	-0.50	± 0.90	-1.20	± 0.33
3RG	-23.23	± 1.57	-8.20	± 1.30	-0.80	± 1.32	-1.40	± 1.72
4RG	-18.08	± 1.45	-11.03	± 1.00	-2.10	± 2.06	-2.10	± 1.06
5RG	-13.50	± 0.76	-9.50	± 1.03	-2.70	± 0.98	-1.50	± 0.38
6RG	-10.43	± 0.95	-9.00	± 1.46	-3.60	± 1.54	-1.60	± 1.67
7RG	-8.30	± 0.58	-11.62	± 1.08	-4.80	± 0.43	-1.10	± 1.03
8RG	-6.90	± 0.41	-16.17	± 0.84	-7.50	± 1.02	-2.90	± 1.21
9RG	-4.90	± 0.34	-12.09	± 0.84	-5.30	± 0.87	-5.40	± 0.80
10RG	-3.40	± 0.57	-9.30	± 0.95	-6.30	± 1.04	-1.20	± 1.71
11RG	-2.70	± 0.27	-7.40	± 0.46	-13.05	± 1.20	-9.20	± 0.73
12RG	-2.20	± 0.14	-4.30	± 0.27	-5.80	± 0.84	-11.68	± 1.25

Table 5. Mean values and confidence intervals of drawdown (LS2).

down (upper panel in Figure 4) first increase close to the generation area and then decrease as the distance from the generation area grows. Nevertheless an extended region is observed to be characterized by almost constant maximum wave runup (i.e. $4<s'<10$) and minimum (maximum in absolute value) wave drawdown (i.e. $s'<10$).

Once the experimental repeatibility has been quantitatively estimated it is possible to use the measurements collected by the sensors placed on the movable system. Given the high spatial resolution, these measurements allow to analyze the free surface elevation time series in the whole experimental domain. In particular, the high density of the sensors in proximity of the shoreline allows to gain insight about the trapping mechanisms that force the waves to propagate around the coast of the island (see Romano et al, 2013). Figure 5 shows the contour plot of the free surface elevation, evaluated at several time steps after the landslide release. Each contour plot has been obtained by linear interpolation of the instantaneous free surface elevation collected around the island.

As far as the elevation time series are concerned a more complete understanding of the overall wave pattern can be depicted. Figure 6 shows maximum wave crest and trough amplitudes of the first (upper panels), the second (middle panels) and third wave (lower panel) at different distances from undisturbed shoreline as a function of angular position (θ). Solid markers indicate measured values at the coast (i.e. runup and drawdown). It can be observed that angular position θ is used instead of dimensionless variable s' as for constant θ (i.e. cross section) the value of s' is not constant.

As far as the first wave is concerned (upper panels in Figure 6), it can be observed that for fixed angular position the maximum crest and trough amplitude is observed at the coast. Moreover, as the distance from the coast (i.e. R) or the distance from the generation area (i.e. $R\theta$) increases the crest and trough amplitudes decrease monotonically. This is not the case for the trailing waves (i.e. second and third waves) for which the maximum amplitudes do not occur at the coast for fixed angular position. Indeed, Figure 6 inspection reveals that there is a spatial shift of the amplitudes, i.e. the maximum amplitudes at the coast (i.e. $R = R_0$, solid markers in Figure 6) occur at higher values of angular position than the maximum amplitude far from the coast (i.e $R > R_0$). Moreover, the maximum amplitudes are not a monotonic function of angular position (as the first wave crest and trough are) as a maximum value is reached at some distance far from the generation area. Therefore, the overall wave propagation around the island is governed by frequency dispersion (Renzi and Sammarco, 2010; Romano et al, 2013). A more detailed description of wave pattern can be addressed by looking at the spatial distribution of crest and trough amplitude around the island. Figure 7 shows the spatial distribution of the crest (upper panels) and trough amplitudes (lower panels) of the first (left panels) and second wave (right panel) obtained by linear interpolation of the experimental data collected by using LS1. The highest amplitudes occur close to the generation area. It can be observed that the maximum amplitude of the first wave crest occurs close to the impact point, while the maximum amplitudes of the first wave trough and of the second wave crest and trough occur at increasing distance. This aspect can be evaluated in more details looking at the time series collected close to the generation area. Along the direc-

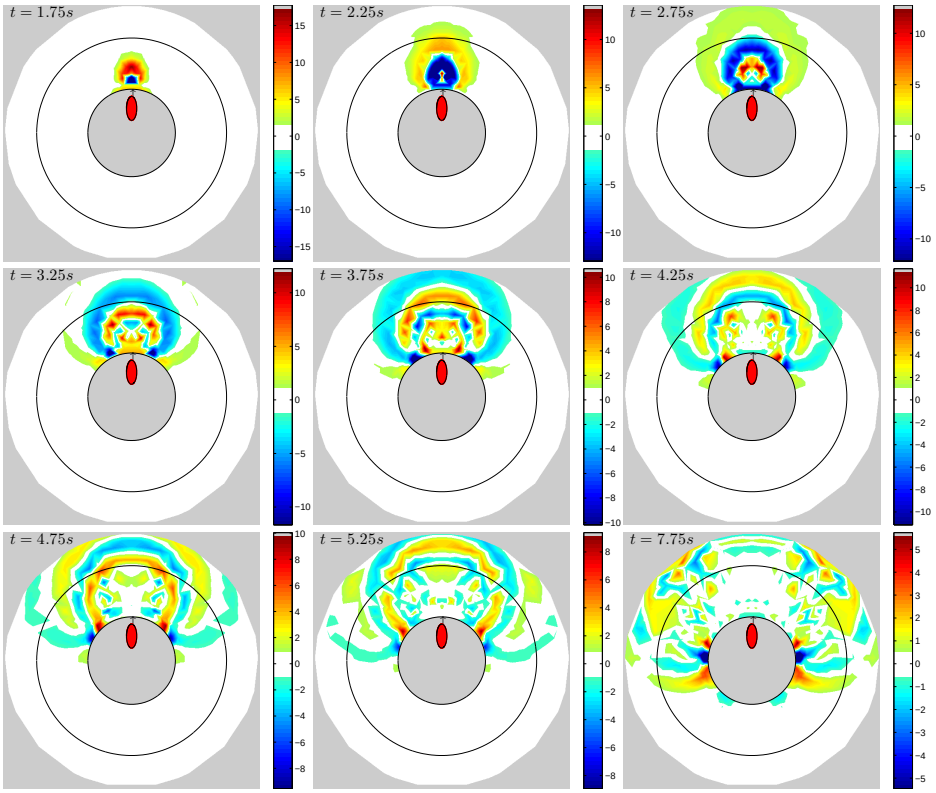


Figure 5. Free surface elevation around the island on the basis of actual measurements at several time steps from the landslide release. Note: in order to magnify the features of the wave propagation, different color scales have been used for each panel.

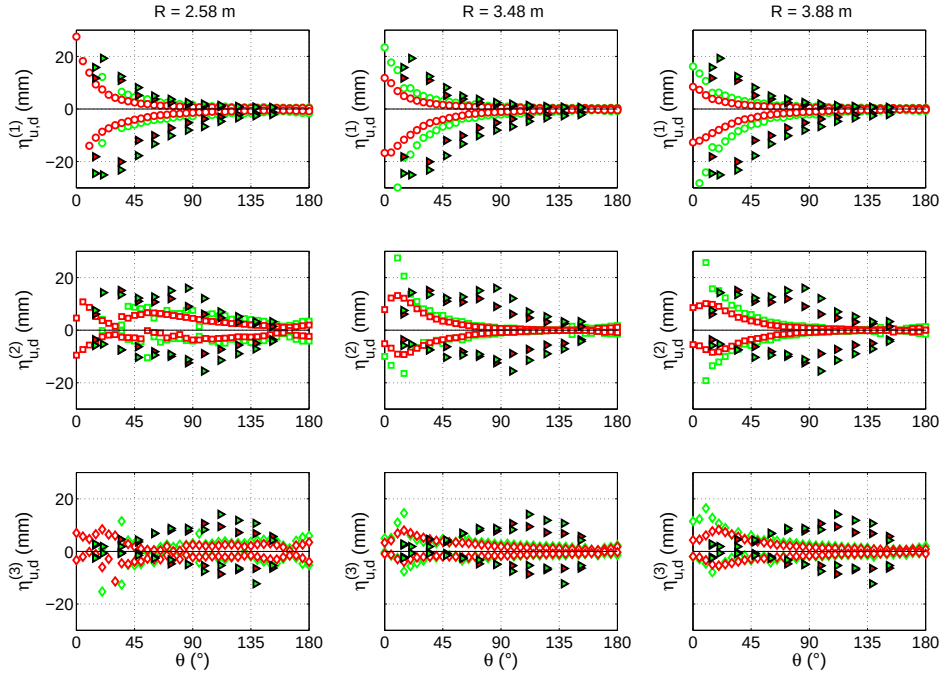


Figure 6. Maximum wave crest and trough amplitudes of the first (upper panels), the second (middle panels) and third wave (lower panel) at different distances (R) from undisturbed shoreline as a function of angular position (θ). Red circles refer to LS1 landslide model, green squares to LS2 landslide model, black edged markers refer to runup and drawdown heights at coast (red markers refer to LS1, while green ones refer to LS2).

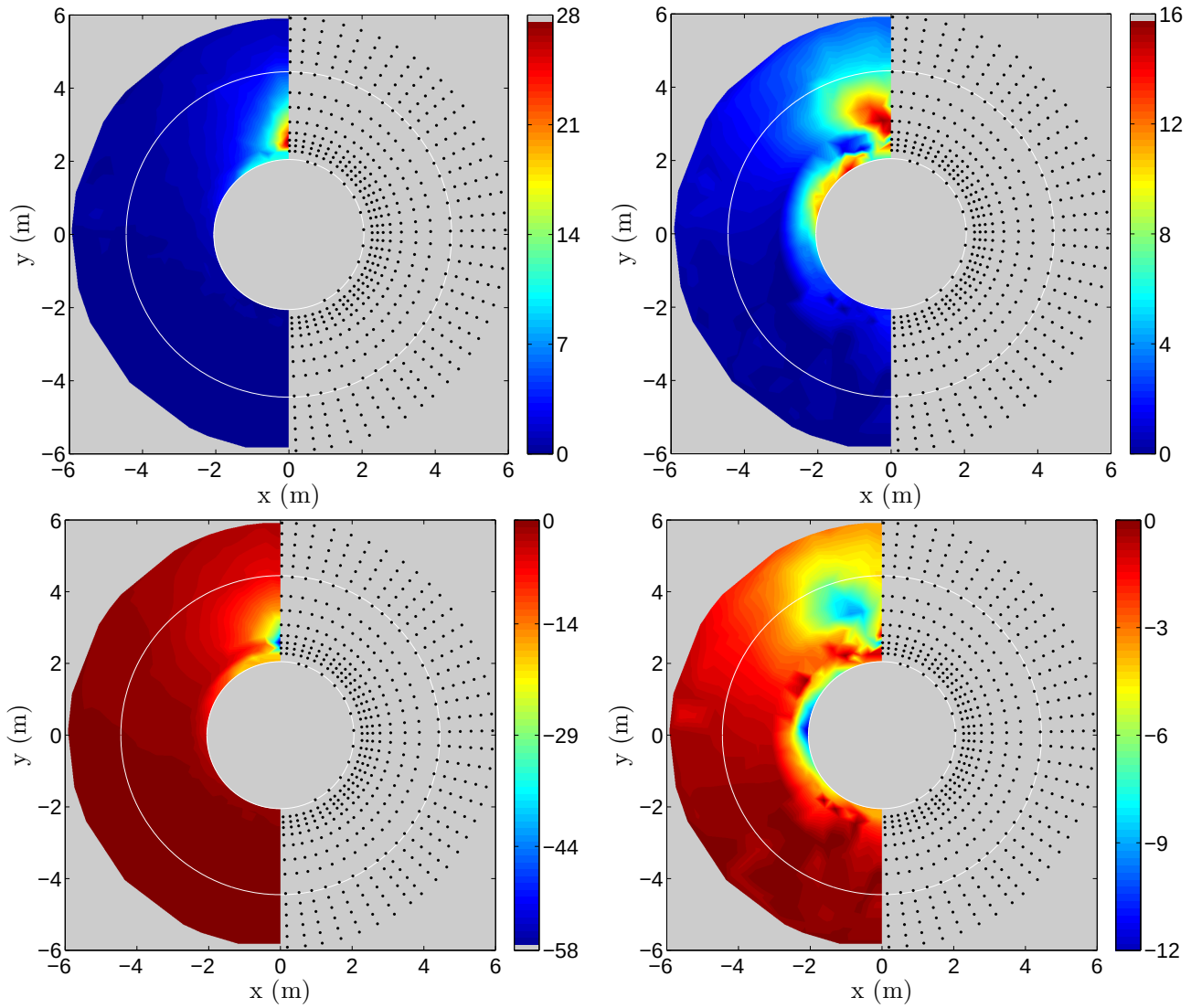


Figure 7. Spatial distribution of crest and trough amplitudes around the island for LS1. Left panels: first wave. Right panels: second wave. Upper panels: wave crests. Lower panels: wave troughs. Note: colorbars are expressed in mm.

tions close to the landslide travel line (i.e. $\theta = 0°$, left panels, and $\theta = 10°$, middle panels, of Figure 8) it can be observed that the first wave exhibits the highest crest and trough amplitudes close to the impact point. As the distance increases the crest and trough amplitudes of the second waves become the highest. Actually the first wave crest and trough can be interpreted as a near-field effect of the wave generation. Indeed, the first crest is generated by the piston-like generation mechanism occuring when the landslide enters the water, while the first trough is generated by the rebound of water and by the interaction of landslide tail with the free surface. As θ increases (i.e. $\theta = 20°$, right panels of Figure 8) the effects of the generation mechanism becomes less important and the wave pattern is governed by propagation phenomena. It is important to stress that only when the propagation mechanisms become important, the maximum amplitudes occur at the coast as already observed in the case of straight coast by Lynett and Liu (2005) and Di Risio et al (2009a).

The existence of trapping and frequency dispersion phenomena is confirmed, even emphasized, by inspecting the Figure 9, that represents the spatial distribution of the wave crest (upper panels) and trough amplitudes (lower panels) of the third (left panels) and fourth wave (right panels) obtained by linearly interpolating the experimental data obtained by using LS1. The third and the fourth waves exhibit their maximum values at the shoreline. The maximum wave crest and trough amplitude of the fourth wave occurs as the angular position

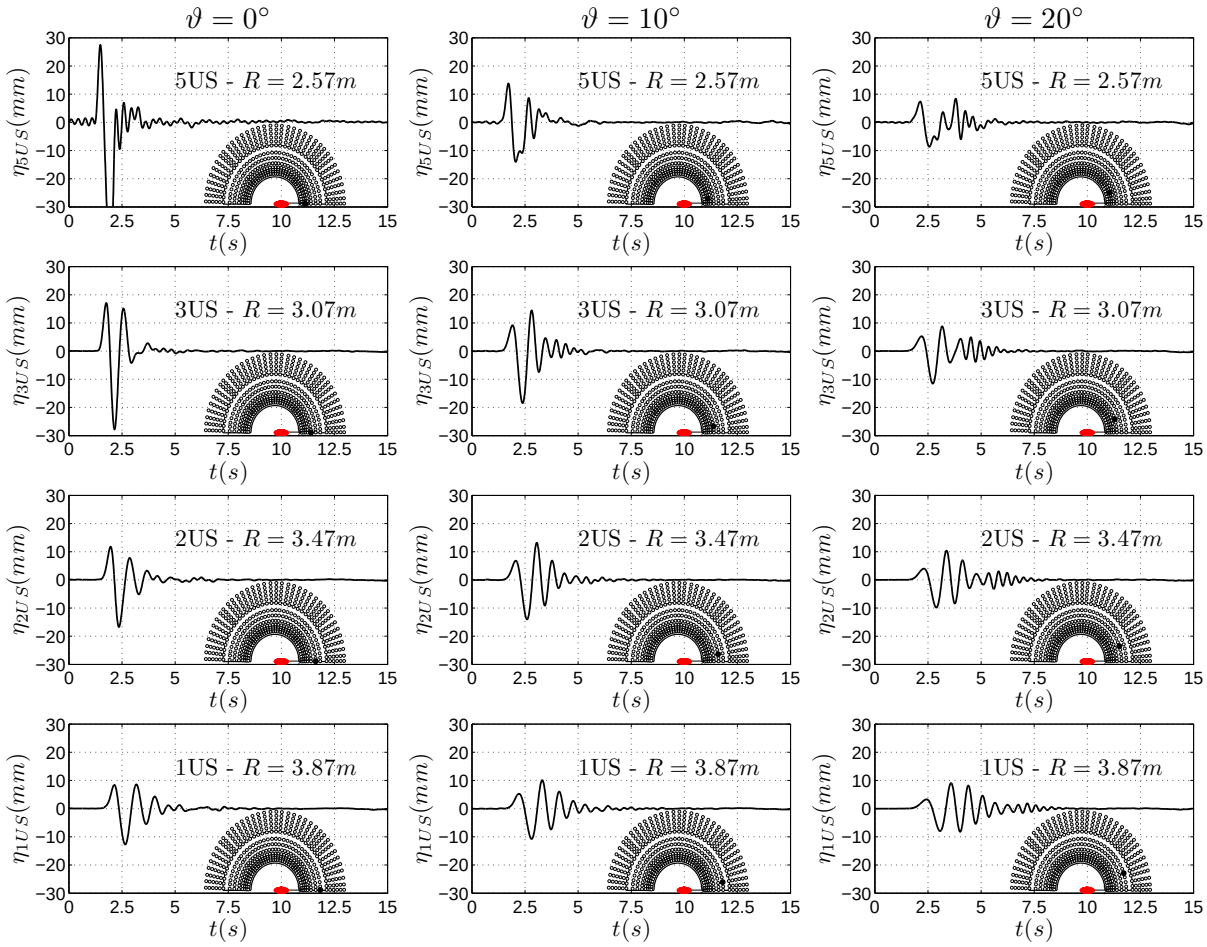


Figure 8. Free surface elevation time series collected by means of the movable system at three angular positions ($\vartheta = 0, 10, 20°$) and at four radial distances ($r = 2.57, 3.07, 3.47, 3.87m$).

ϑ, from the generation area, is almost 180° (i.e., the rear side of the island).

4.4 Wave periods and celerities

The wave periods have been estimated by means of both time domain (zero-crossing analysis) and frequency domain (spectral analysis) standard techniques.

As far as the individual first three waves of the generated train are concerned, Figure 10 shows the wave periods as a function of the dimensionless variable s' ($= R\theta/b$). It is almost clear that the first wave period, even if rather dispersed, increases as the distance from generation area grows. The periods of the trailing waves exhibit lower dispersion and it is possible to observe clear differences between radiating waves period and the period of the waves that propagate along the coast of the island, with the former smaller than the latter. It can be argued that two different wave systems occur and each of them follows its own dispersion relation as demonstrated by Romano et al (2013) by using the wavenumber-frequency analysis. Moreover, it appears that the period of the radiating waves remains almost constant and equal to about 1.0 s, whilst the period of the waves propagating along the coast is of the order of 2.0 s.

As far as the wave celerities are concerned, Figure 11 shows the mean celerities along constant s' as a function of dimensionless distance from the coastline ($R/R_0 \geq 1$). The celerities were estimated by using the observed time delay of arrival time at different points at the same distance from coastline with different angular position. It can be observed that the celerity increases as the distance from the coastline increases. Close to the coast ($R/R_0 \simeq 1$) the mean wave celerity is about 0.85 m/s, whilst at R/R_0=1.89 ($R = 3.88$ m) the mean wave celerity grows up to about 1.80 m/s. On the basis of the observed period it is possible to estimate the wave length close to the coast as equal to 1.70 m (i.e. $L = CT$), almost consistent with the observed values of Di Risio et al (2009b). It is also possible to estimate the wave length of the radiating

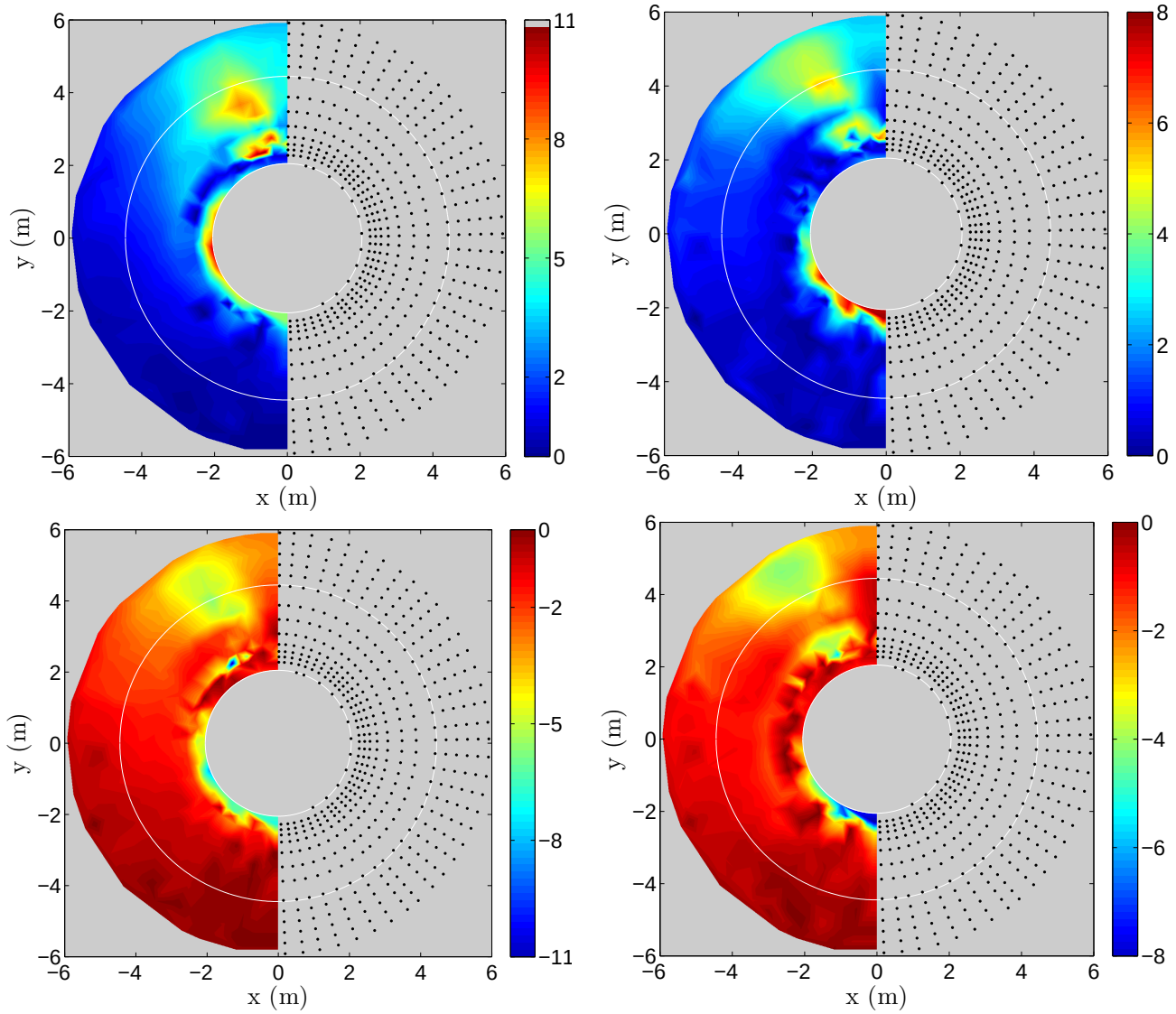


Figure 9. Spatial distribution of crest and trough amplitudes around the island for LS1. Left panels: third wave. Right panels: fourth wave. Upper panels: wave crests. Lower panels: wave troughs. Note: colorbars are expressed in mm.

waves as about 3.60 m.

It is interesting to evaluate the mean arrival times of the run-up waves along the shoreline. Arrival times are shown in Figure 12 as a function of the dimensionless distance s'. Positive values of s' refer to experimental results observed for LS1, negative ones are referred to LS2 data. For each run-up gauge (i.e., at a fixed value of s') the lower black markers identify the time at which the first wave of the tsunami occurs, the red markers identify the time at which the maximum of the wave packet occurs, and finally the upper black markers identify the time at which the fifth wave ends. As s' increases, the time at which the maximum of the wave packet occurs increases as well; in particular the arrival time tends to move from the arrival time of the first wave toward the ones of the following waves (i.e., second, third, etc.). This feature confirms that frequency dispersion is prevalent in wave propagation alongshore. As pointed out by Romano et al (2013), the waves propagate as a 0th-order edge waves packet.

5. Concluding remarks and ongoing research

The paper presents a new set of three-dimensional experiments reproducing tsunamis generated by subaerial landslides sliding down the flank of a conical island. The experimental investigation was carried out by employing a special movable system that allows to achieve high spatial resolution, comparable to the resolution of

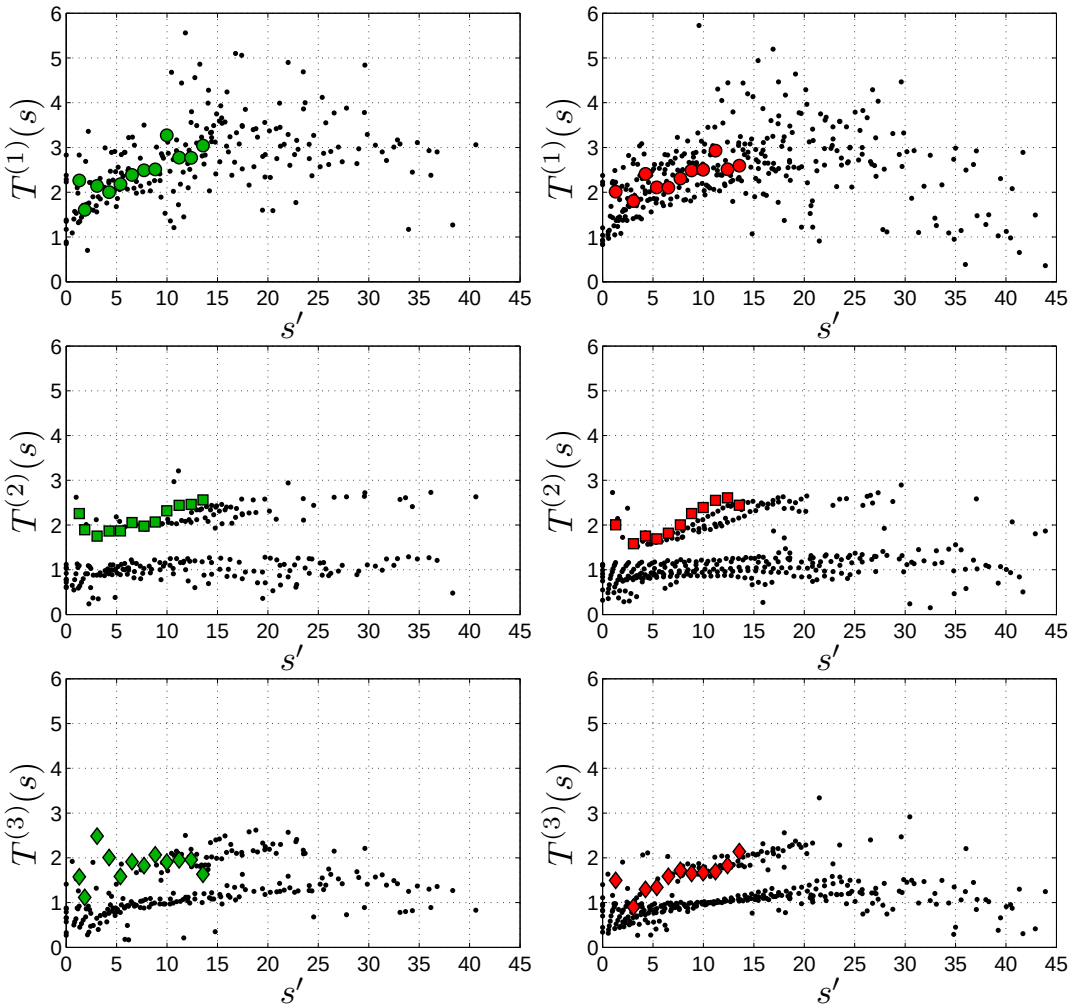


Figure 10. Individual wave periods of the first three waves measured by the movable system and the run-up gauges. Note : black points refer to the wave periods of the waves measured by the movable system, while the solid markers (green and red) refer to the wave periods of the run-up waves. Right panels refer to LS1, while left ones refer to LS2.

numerical results. Then, the experimental data are intended to be useful to gain insight about the physical phenomenon at hand and to be used as a benchmark for mathematical and numerical models validation. A detailed analysis of the landslide motion was performed and hydrodynamic coefficients were estimated on the basis of observed landslide displacements in order to provide reliable tools to define boundary conditions to be used in numerical models.

A measure of the data uncertainty was estimated. Analysis on free surface elevation shows that near the impact area the wave features are dependent upon the near-field wave generation process and the highest wave amplitude occurs in front of the impact area. When propagation mechanisms become the governing phenomena, the highest wave amplitudes occur at the coast. It is almost clear that two different system of waves are generated. The first one propagates along the coast and according to Romano et al (2013) it is composed of 0th-order edge waves, while the second one radiates offshore. Wave periods, celerities and wave length of the two systems are rather different. Close to the coast wave periods are higher and wave celerities are lower if compared to the radiating waves. The landslides thickness affects significantly only the wave amplitudes, especially in the near field; for instance, if one considers the runup of the first wave close to the generation area it can be seen that the one induced by LS2 is almost twice than that observed by using LS1, whilst the drawdown of the same wave caused by the two landslide models exhibit smaller differences. For the wave periods (and celerities) it can be observed a weak dependence upon

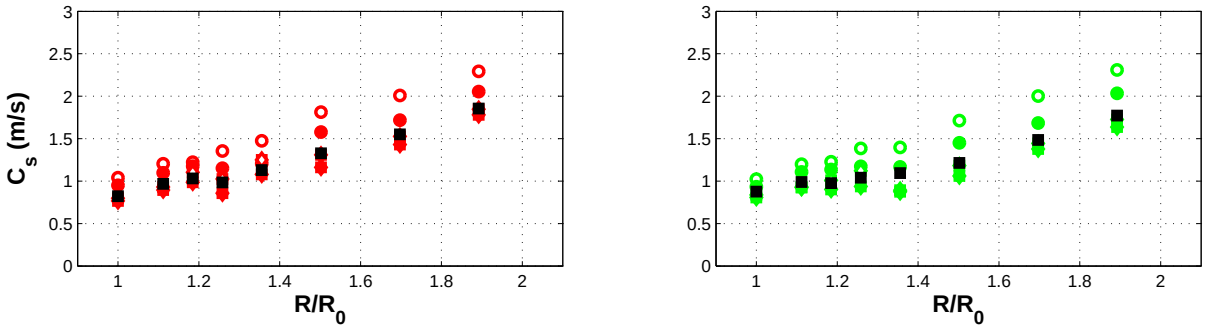


Figure 11. First wave crest (empty circles), first wave trough (solid circles),second wave crest (empty squares), second wave trough (solid squares), third wave crest (empty diamonds) and third wave trough (solid diamonds) celerities for LS1 (left panel) and LS2 landslide (right panel). Black solid markers indicate mean wave celerities.

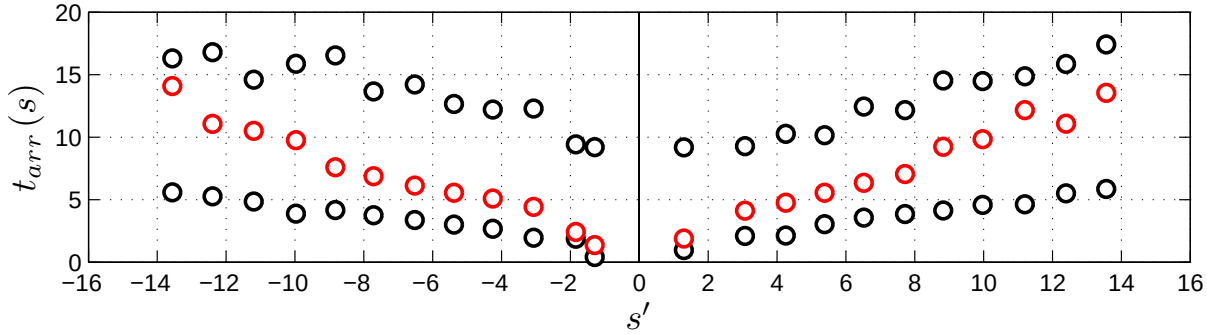


Figure 12. Mean arrival times of the run-up waves along the shoreline as a function of s'. Note: lower black markers refer to the time at which the tsunami begins; red markers identify the time at which the maximum of the packet occurs; upper black markers identify the time at which the fifth wave ends.

the landslide volume. The experimental data presented in the paper are available on request.

Acknowledgements

The research described in this paper is funded by the Italian Ministry of Research within the PRIN2007 research project "Development and validation of hydraulic and geologic tools for supporting a Tsunami Early Warning System. Implementation to the Stromboli (Eolie) landslide case.". The author wish to thanks Eng. Michele Di Lazzaro (University of Roma Tre, Italy) that provided the ultrasound sensors. Mario Nardi and Lucio Matergia, the technicians of LIAM (University of L'Aquila), are acknowledged for their skills in building physical models.

References

Bellotti G, Di Risio M, De Girolamo P (2009) Feasibility of tsunami early warning systems for small volcanic islands. Natural Hazards and Earth System Science 9(6):1911–1919

Briggs M, Synolakis C, Harkins G, Hughes S (1995b) Large scale three-dimensional laboratory measurements of tsunami inundation. Advances In Natural And Technological Hazards Research 4:129–150

Briggs M, Synolakis C, Harkins G, Green D (1995a) Laboratory Experiments of tsunami runup on a circular island. Pure And Applied Geophysics 144(3-4):569–593, DOI {10.1007/BF00874384}

Cecioni C, Romano A, Bellotti G, Di Risio M, de Girolamo P (2011) Real-time inversion of tsunamis generated by landslides. Nat Hazards Earth Syst Sci 11:2511–2520

Cho YS, Liu PLF (1999) Crest-length effects in nearshore tsunami run-up around islands. J Geophys Res 104(C4):7907–7913, DOI 10.1029/1999JC900012

Cho YS, Park KY, Lin TH (2004) Run-up heights of nearshore tsunamis based on quadtree grid system. Ocean Engineering 31(8 - 9):1093 – 1109, DOI 10.1016/j.oceaneng.2003.10.011

Di Risio M, Sammarco P (2008) Analytical modeling of landslide-generated waves. Journal of waterway, port, coastal, and ocean engineering 134(1):53–60

Di Risio M, De Girolamo P, Beltrami G (2011) Forecasting landslide generated tsunamis: a review. The Tsunami Threat - Research and Technology, Nils-Axel Marner (Ed.)

Di Risio M, Bellotti G, Panizzo A, De Girolamo P (2009a) Three-dimensional experiments on landslide generated waves at a sloping coast. Coastal Engineering 56(5-6):659–671, DOI {10.1016/j.coastaleng.2009.01.009}

Di Risio M, De Girolamo P, Bellotti G, Panizzo A, Aristodemo F, Molfetta MG, Petrillo AF (2009b) Landslide-generated tsunamis runup at the coast of a conical island: New physical model experiments. Journal of Geophysical Research-Oceans 114, DOI {10.1029/2008JC004858}

Enet F, Grilli ST (2007) Experimental study of tsunami generation by three-dimensional rigid underwater landslides. Journal Of Waterway Port Coastal And Ocean Engineering-ASCE 133(6):442–454, DOI {10.1061/(ASCE)0733-950X(2007)133:6(442)}

Fritz HM, Mohammed F, Yoo J (2009) Lituya bay landslide impact generated mega-tsunami 50th anniversary. Pure and Applied Geophysics 166(1-2):153–175

Grilli ST, Watts P (2003) Underwater Landslide Shape, Motion, Deformation, and Tsunami Generation. In: EGS - AGU - EUG Joint Assembly, p 13216

Johnson RS (2007) Edge waves: theories past and present. Philosophical Transactions Of The Royal Society A-Mathematical Physical And Engineering Sciences 365(1858):2359–2376, DOI {10.1098/rsta.2007.2013}

Liu PLF, Yeh H (1996) The generation of edge waves by a wave-maker. Physics Of Fluids 8(8):2060–2065, DOI {10.1063/1.869008}

Liu PLF, Cho YS, Briggs MJ, Kanoglu U, Synolakis CE (1995) Runup of solitary waves on a circular island. Journal of Fluid Mechanics 302:259–285, DOI 10.1017/S0022112095004095

Liu PLF, Yeh H, Lin P, Chang K, Cho Y (1998) Generation and evolution of edge-wave packets. Physics Of Fluids 10(7):1635–1657, DOI {10.1063/1.869682}

Lynett P, Liu PLF (2005) A numerical study of the run-up generated by three-dimensional landslides. Journal of Geophysical Research-Oceans 110(C3), DOI {10.1029/2004JC002443}

Miller D (1960) Giant Waves in Lituya Bay, Alaska: A Timely Account of the Nature and Possible Causes of Certain Giant Waves, with Eyewitness Reports of Their Destructive Capacity. Professional paper, U.S. Government Printing Office

Mohammed F, Fritz HM (2012) Physical modeling of tsunamis generated by three-dimensional deformable granular landslides. Journal of Geophysical Research: Oceans (1978–2012) 117(C11)

Montagna F, Bellotti G, Di Risio M (2011) 3d numerical modeling of landslide-generated tsunamis around a conical island. Natural hazards 58(1):591–608

Panizzo A, De Girolamo P, Di Risio M, Maistri A, Petaccia A (2005) Great landslide events in italian artificial reservoirs. Natural Hazards and Earth System Science 5(5):733–740, DOI 10.5194/nhess-5-733-2005

Pelinovsky E, Poplavsky A (1996) Simplified model of tsunami generation by submarine landslides. Physics and Chemistry of The Earth 21(1 - 2):13 – 17

Renzi E, Sammarco P (2010) Landslide tsunamis propagating around a conical island. Journal of Fluid Mechanics 650:251–285, DOI {10.1017/S0022112009993582}

Romano A, Bellotti G, Di Risio M (2013) Wavenumber–frequency analysis of the landslide-generated tsunamis at a conical island. Coastal Engineering 81:32–43

Russell JS (1845) Report on waves. In: 14th meeting of the British Association for the Advancement of Science, pp 311–390

Sammarco P, Renzi E (2008) Landslide tsunamis propagating along a plane beach. Journal of Fluid Mechanics 598:107–119, DOI {10.1017/S0022112007009731}

Synolakis CE, Bardet JP, Borrero JC, Davies HL, Okal EA, Silver EA, Sweet S, Tappin DR (2002) The slump origin of the 1998 papua new guinea tsunami. Proceedings of the Royal Society of London Series A: Mathematical, Physical and Engineering Sciences 458(2020):763–789, DOI 10.1098/rspa.2001.0915

Tinti S, Manucci A, Pagnoni G, Armigliato A, Zaniboni F (2005) The 30 December 2002 landslide-induced tsunamis in Stromboli: sequence of the events reconstructed from the eyewitness accounts. Natural Hazards and Earth System Science 5(6):763–775, URL `http://hal.archives-ouvertes.fr/hal-00299290`

Ursell F (1952) Edge waves on a sloping beach. Proceedings of the Royal Society of London Series A Mathematical and Physical Sciences 214(1116):79–97, DOI 10.1098/rspa.1952.0152

Watts (1998) Wavemaker curves for tsunamis generated by underwater landslides. Journal of Waterway, Port, Coastal, and Ocean Engineering 124(3):127–137, DOI 10.1061/(ASCE)0733-950X(1998)124:3(127)

Watts P (2000) Tsunami features of solid block underwater landslides. Journal of Waterway, Port, Coastal, and Ocean Engineering 126(3):144–152, DOI 10.1061/(ASCE)0733-950X(2000)126:3(144)

Watts P, Grilli S, Tappin D, Fryer G (2005) Tsunami generation by submarine mass failure. ii: Predictive equations and case studies. Journal of Waterway, Port, Coastal, and Ocean Engineering 131(6):298–310, DOI 10.1061/(ASCE)0733-950X(2005)131:6(298)

Yeh H, Liu PLF, Briggs M, Synolakis CE (1994) Propagation and amplification of tsunamis at coastal boundaries. Nature 372(6504):353–355, DOI 10.1038/372353a0

Yim S, Yuk D, Panizzo A, Di Risio M, Liu PF (2008) Numerical simulations of wave generation by a vertical plunger using rans and sph models. Journal of waterway, port, coastal, and ocean engineering 134(3):143–159